www.nature.com/scientificreports

SCIENTIFIC REPORTS

Composite Photocatalysts Containing $BiVO_4$ for Degradation of Cationic Dyes

Received: 30 May 2017
Accepted: 26 July 2017

Kanlaya Pingmuang[1,2], Jun Chen[1], Wiyong Kangwansupamonkon[3], Gordon G. Wallace[1], Sukon Phanichphant[2] & Andrew Nattestad[1]

The creation of composite structures is a commonly employed approach towards enhanced photocatalytic performance, with one of the key rationales for doing this being to separate photoexcited charges, affording them longer lifetimes in which to react with adsorbed species. Here we examine three composite photocatalysts using either WO_3, TiO_2 or CeO_2 with $BiVO_4$ for the degradation of model dyes Methylene Blue and Rhodamine B. Each of these materials (WO_3, TiO_2 or CeO_2) has a different band edge energy offset with respect to $BiVO_4$, allowing for a systematic comparison of these different arrangements. It is seen that while these offsets *can* afford beneficial charge transfer (CT) processes, they can also result in the deactivation of certain reactions. We also observed the importance of localized dye concentrations, resulting from a strong affinity between it and the surface, in attaining high overall photocatalytic performance, a factor not often acknowledged. It is hoped in the future that these observations will assist in the judicious selection of semiconductors for use as composite photocatalysts.

Bismuth vanadate ($BiVO_4$) has attracted much attention as a highly responsive, visible-light driven, photocatalyst due to its comparatively narrow band gap (E_G) energy of 2.4 eV, (as compared to TiO_2, which remains a benchmark, with an E_G of 3.0–3.2 eV). $BiVO_4$ has been widely used in the photocatalytic degradation of organic compounds in waste water as well as for O_2 evolution under sunlight irradiation[1–4].

One of limitations of the photocatalytic efficiency in $BiVO_4$ is the recombination of photogenerated electrons and holes, with the free carrier life time reported to be about 40 ns by Abdi *et al.*[5]. In order to enhance these lifetimes, the creation of electronic barriers, facilitating spatial separation of the photogenerated electrons and holes, has been embraced by researchers as they can retard this recombination, providing more opportunities for free holes and electrons to participate in reduction and/or oxidation reactions, such as for the degradation of organic materials[4,6]. Doping semiconductors, either with metal or non-metals, has also been demonstrated to be an effective method for enhancing photocatalytic performance[4,6,7]. The composite approach relies on exploiting band-edge offsets, directing the electrons and holes into different materials, thereby providing spatial separation.

Recently, many publications have coupled $BiVO_4$ with other metal oxides such as Bi_2O_3[8,9], V_2O_5[10,11], TiO_2[12,13], WO_3[11,14–16], CdS[17], $CuCr_2O_4$[18] and $CuWO_4$[19], for water purification and water spitting applications. The results show that the semiconductor composite photocatalysts were more active than individual catalysts for all photocatalytic degradation of organic pollutants - notwithstanding the fact that it is less likely that composites providing lower photocatalytic performances would be published. While most of these reports on composite catalysts acknowledge the role of band edge offsets, detailed investigations of reaction mechanisms are often not undertaken, nor has the nature of these energy offsets been thoroughly scrutinized[8,10,13,18,20].

Here we present a systematic study, pairing $BiVO_4$ with three different metal oxide semiconductors to create different offsets scenarios. $CeO_2/BiVO_4$, $TiO_2/BiVO_4$ and $WO_3/BiVO_4$ provide these different valence band (VB) and conduction band (CB) edge offsets, with the CB and VB potential edges of $BiVO_4$ being more positive than those of CeO_2, in between those of TiO_2, and more negative than those of WO_3; as shown in Fig. 1[6,7,20–22]. These

[1] ARC Centre of Excellence for Electromaterials Science, Intelligent Polymer Research Institute, Australian Institute of Innovative materials, Innovation Campus, University of Wollongong, Fairy Meadow, NSW, 2519, Australia. [2] Department of Chemistry and Materials Science Research Center, Faculty of Science, Chiang Mai University, 239 Huay Kaew Road, Muang District, Chiang Mai, 50200, Thailand. [3] National Nanotechnology Center, Thailand, 130 Thailand Science Park, Paholyothin Road, Pathumthani, 12120, Thailand. Correspondence and requests for materials should be addressed to A.N. (email: anattest@uow.edu.au)

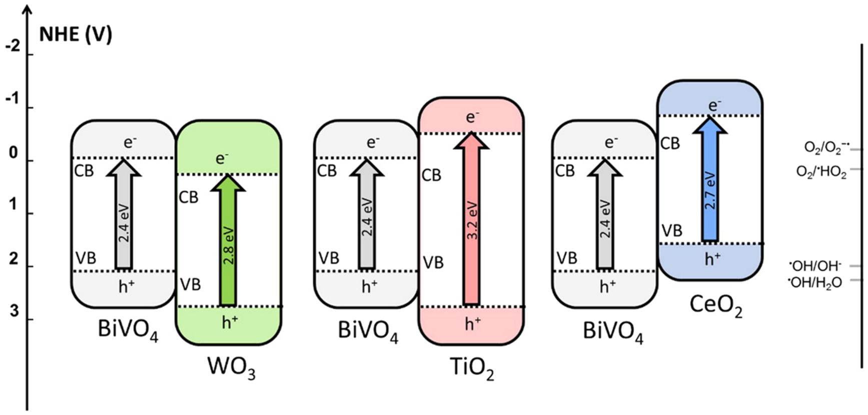

Figure 1. Schematic diagrams of the energy band structures of coupling $WO_3/BiVO_4$, $TiO_2/BiVO_4$ and $CeO_2/BiVO_4$ composites, based on literature values (band edge energy values taken from[6, 7, 20–22]).

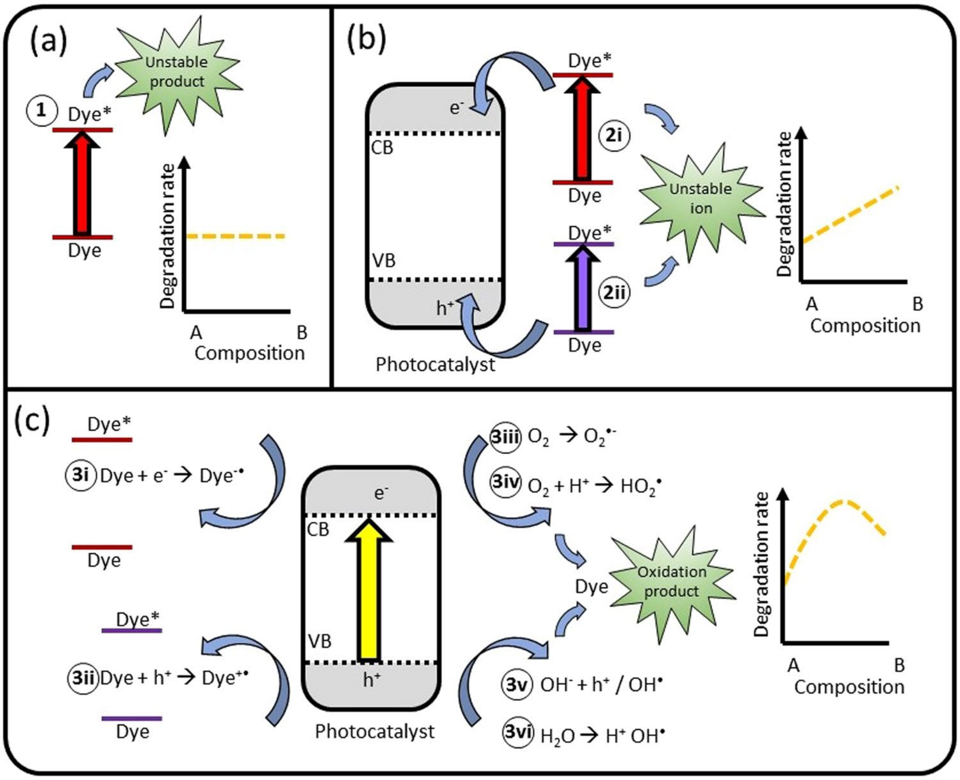

Figure 2. Photodegradation mechanisms. (**a**) Direct degradation by (1) direct photolysis. (**b**) Dye-sensitization leading to degradation through either electron (2i) or hole injection (2ii). (**c**) Indirect degradation of dyes by various photocatalytic reactions. (3i) and (3ii) involve direct oxidation/reduction of the dye by the photoexcited catalyst, while (3ii–3vi) proceed via radical intermediates. For each class of catalytic mechanisms, a schematic (yellow dotted line) represents how they are expected to vary with composition, with further explanation provided in text.

materials are selected based on literature values, as it is expected that this will result in different charge transfer (CT) processes being able to take place. In each case $BiVO_4$ has the narrowest bandgap and hence the broadest absorption, so the total amount of light harvested is consistent for each of the composites. As the above band edge potentials are obtained from different sources, and measured under different conditions, optical band gap and Mott-Shotkey measurements are conducted in order to confirm the predicted offsets.

A number of mechanisms for photocatalytic degradation of dyes by semiconductors are summarised in Fig. 2, including (1) direct photolysis of dyes (2) dye photosensitization (*i.e*. charge injection from a photoexcited dye leaving unstable dye anion/cation) and (3) photocatalytic degradation of dyes attack by radical generated by photoexcitation of semiconductor (SC)[22–25]. Typically direct photolysis is very slow, impractical as a means to remove organic contaminants from waste water, and indeed is the reason why researchers look towards using photocatalysts to enhance degradation rates[24]. Figure 2a shows schematically how mechanism (1) operates. It is expected that mechanism (1) should be independent of the catalyst used, or the percentage of each catalysts used in composite systems, provided there is no light harvesting competition (Methylene Blue, MB, absorbs most strongly at 664 nm, well beyond the absorption onset of $BiVO_4$).

There are two variants of mechanism (2) which may occur, depending on the redox potentials of the dye compared to the band edges of the catalyst. Mechanism (2i) is photoanodic sensitization, with the excited dye injecting an electron into the semiconductor leading to an oxidized radial cation ($Dye^{+\bullet}$), while (2ii) is photocathodic sensitization, generating a reduced radical dye ($Dye^{-\bullet}$). Furthermore, these injected charges may lead to generation of other radical species. The chemical driving force between the dye redox potentials and those of the semiconductor will largely determine the rate of mechanism (2), and as such, with everything else being equal, should be proportional to the geometric mean of the components in composites.

Degradation mechanisms (3i-vi), shown in Fig. 2b, rely on photoexcitation of the semiconductor. Generated h^+ and e^- pairs (in the VB and CB of the semiconductor respectively) then react either directly (3i and 3ii) or generate radical intermediate species, which can degrade organic species such as the aforementioned dyes (3iii–3vi). There are a number of reactions which may take place, once again depending on the energies of the semiconductor band edges and the environment in which it exists[22, 26–28]:

(3i) $e^-_{CB} + Dye \rightarrow Dye^{-\bullet}$ (Dye dependent)
(3ii) $h^+_{VB} + Dye \rightarrow Dye^{+\bullet}$ (Dye dependent)
(3iii) $e^-_{CB} + O_{2(aq)} \rightarrow O_2^{-\bullet}$ (-0.18 V *vs.* NHE)
(3iv) $e^-_{CB} + O_{2(aq)} + H^+ \rightarrow HO_2^{\bullet}$ ($+0.10$ V *vs.* NHE)
(3v) $h^+_{VB} + OH^- \rightarrow OH^{\bullet}$ ($+1.99$ V *vs.* NHE)
(3vi) $h^+_{VB} + H_2O \rightarrow H^+ + OH^{\bullet}$ ($+2.73$ V *vs.* NHE)

Thus, the degradation will greatly depend on the adsorption of the dye, O_2, OH^-, H^+ and/or H_2O on the surface of semiconductor. Photogenerated e^- and h^+ can of course also recombine (either radiatively or non-radiatively) within the material. It is therefore beneficial to increase the lifetimes of these species to increase the probability that they will participate in one of the above reactions (3i-vi). Mechanisms in this third family may display a synergistic response, where composites can lead to higher reaction rates than either of the two component materials.

In addition to examining rates of photocatalytic degradation for the different heterostructures, in this study, we also examine the mechanisms. This is done in two ways; firstly, through reactive species quenching studies, to differentiate between mechanisms involving $OH^{\bullet}$, $O_2^{\bullet -}$, h^+, e^- and secondly with action spectra, taken to deconvolute the responses of the constituent materials. Additionally, a range of physical characterization techniques were employed, such as X-Ray Diffraction (XRD), X-ray photoelectron spectroscopy (XPS), Mott-Schottky experiments, and Scanning Electron Microscopy (SEM).

Rhodamine B (RhB) and Methylene Blue (MB) are commonly used as model dyes for photodegradation experiments, being broadly representative of organic compounds in their class[22, 24], while being strongly light absorbing (making the remaining concentration easy to monitor by UV-Vis spectroscopy). In addition, since they absorb visible light, mechanisms (1) - direct photolysis[25], and (2) - sensitization may occur in these systems, in addition to (3). Photoexcited MB can undergo a one electron reduction by other MB molecules to produce *Leuco*-methylene blue ($MB/MB^{\bullet -} = -0.23$ V *vs.* NHE)[23].

Results

$WO_3/BiVO_4$, $TiO_2/BiVO_4$ and $CeO_2/BiVO_4$ composite powders, along with the respective pure materials, were synthesized by wet chemical methods with different mole ratios (1:4, 2:3, 1:1, 3:2 and 4:1), and used to produce photocatalyst films on glass by a doctor blading method[29]. In a preliminary study, the photocatalytic activities these investigated by degradation of MB and RhB under simulated solar irradiation. The concentration of remaining of dye shows a first order degradation relationship with respect to time, which can be fitted to the Langmuir-Hinshelwood (LH) kinetic model[30] (shown in Fig. S1). It was found that 1:4, 1:1 and 2:3 were the optimal ratios of WO_3:$BiVO_4$, TiO_2:$BiVO_4$ and CeO_2:$BiVO_4$ respectively for both MB and RhB under visible light irradiation, (Fig. S2). It should be noted that in each case, the composites outperformed the individual component materials, as predicted for type (3) mechanisms. These optimal ratios were chosen for further investigations, and are referred to simply as $WO_3/BiVO_4$, $TiO_2/BiVO_4$ and $CeO_2/BiVO_4$, respectively from this point on.

The crystal structures of the composites were characterized by XRD, as shown in Fig. 3, with each XRD pattern showing only characteristic diffraction peaks of monoclinic $BiVO_4$ and either monoclinic WO_3, tetragonal TiO_2 (anatase) or cubic fluorite CeO_2 respectively, as expected. XRD patterns of the individual component materials can also be found in Fig. S3. Furthermore, XPS analysis was carried out to study the surface chemical composition of the above composites, and take a more detailed look at the interactions between $BiVO_4$ and the other metal oxide in each of the composites, as shown in Figs S4–S6. Due to proximity, electronic interactions were observed for these composites when examined by XPS[30–34]. It was therefore concluded, from XRD and XPS that these systems were intimately formed composites, but did not contain any significant doping or any a mixed oxide phases.

The morphologies of $WO_3/BiVO_4$, $TiO_2/BiVO_4$ and $CeO_2/BiVO_4$ composite powders and films were investigated using SEM (Fig. 4), with films shown to be highly porous and approximately the same thickness, ~2.8 μm, by cross-sectional SEM (Fig. 4c,f,i), in line with profilometry values mentioned previously. In each case, the two component materials appear to be well distributed among each other, as it particularly evident in the Energy Dispersive X-Ray Spectroscopy (EDS) maps. EDS data shows Bi and V tracking with one another, as expected, while other regions are rich in either W, Ti or Ce respectively, corresponding to WO_3, TiO_2 or CeO_2 particles in

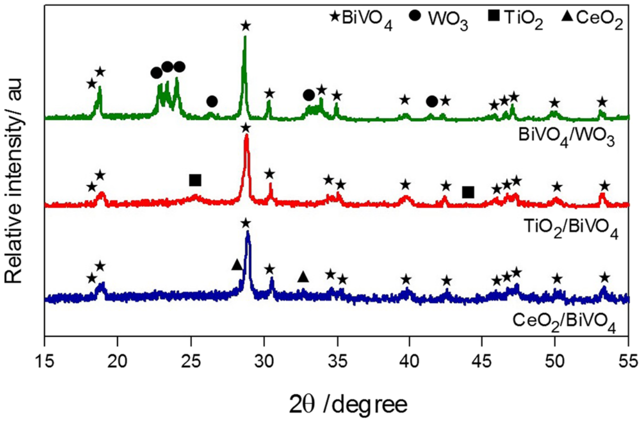

Figure 3. XRD patterns of composite photocatalysts.

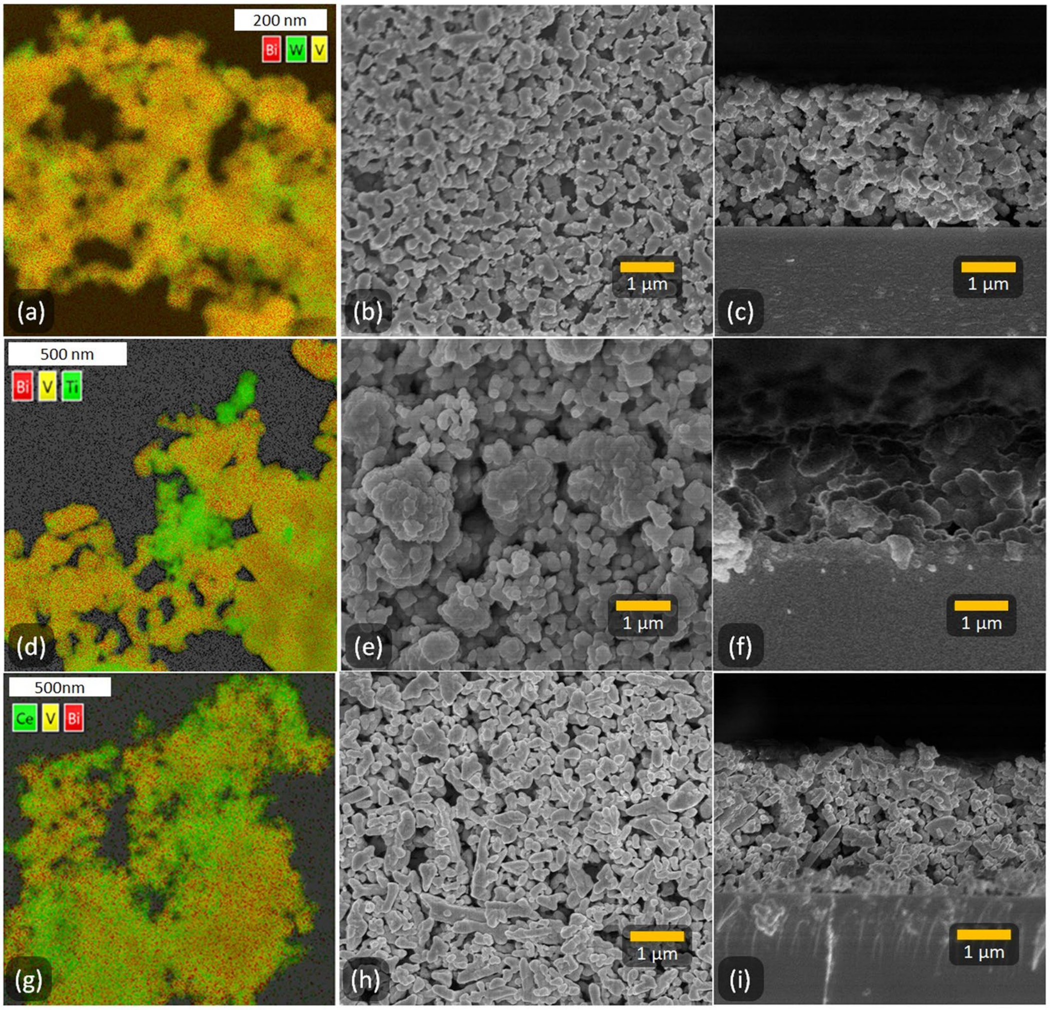

Figure 4. EDS maps of nanocomposite powders (**a**,**d**,**g**), along with top down (**b**,**e**,**h**) and cross-sectional (**c**,**f**,**i**) SEM images of the composite films of (**a**–**c**), $WO_3/BiVO_4$, (**d**–**f**) $TiO_2/BiVO_4$, and (**g**–**i**), $CeO_2/BiVO_4$, respectively.

the relevant composites. The scale of these differences suggests again that there are well-formed composites, with each containing image (Fig. 4a,d,g) two distinct materials in close proximity to one another. Further analysis of EDS (Figs S7–S9) is included in the supplemental information, along with TEM images (Fig. S10).

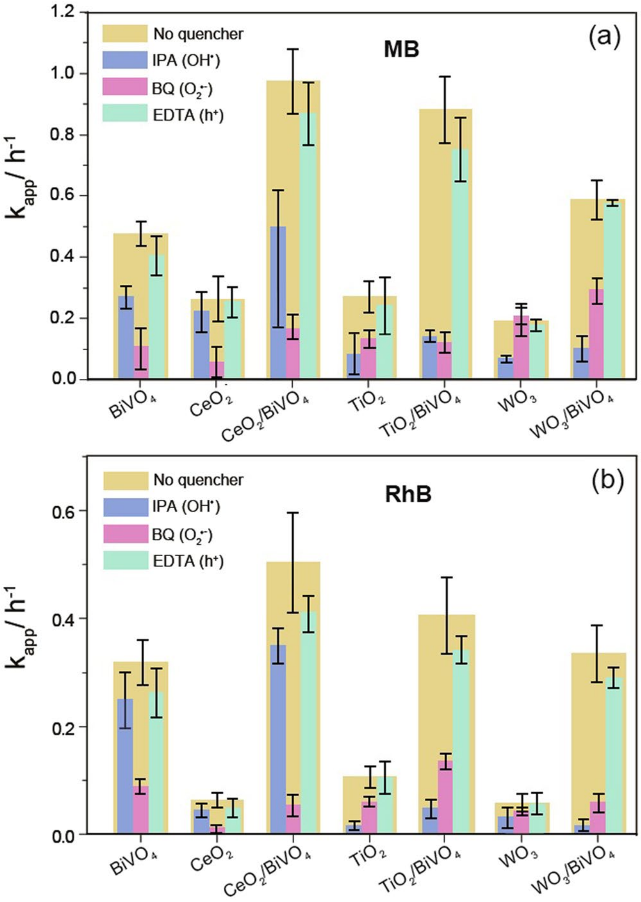

Figure 5. Observed pseudo first order rate constants (k_{app}) of photodegradation of (**a**) MB and (**b**) RhB by using different photocatalysts with and without scavengers under simulated solar irradiation.

The mechanisms of photocatalytic degradation of MB and RhB, by $BiVO_4/WO_3$ $BiVO_4/TiO_2$ and $BiVO_4/CeO_2$ were investigated by an indirect chemical probe method, with active species scavengers (see Fig. 5). Normally in the photocatalytic oxidation process, organic species (notably double bonds) are attacked by active species, including holes (h^+), hydroxyl radical ($HO^•$) and/or superoxide anion radical ($O_2^{•-}$)[35–40]. As mentioned, IPA, BQ and EDTA were introduced into photocatalysis experiment as scavengers of $HO^•$, $O_2^{•-}$ and h^+, respectively. The photocatalytic degradation rate constant (k_{app}) for the composites and pure materials (both for MB (Fig. 5a) and RhB (Fig. 5b)), with the above quenchers (1 mM) were investigated under simulated solar irradiation.

The addition of BQ almost completely quenched the dye degradation of both the pure $BiVO_4$ and CeO_2 indicating that $O_2^{•-}$ is the major active species in these systems. For the photodegradation of dyes with the TiO_2 and WO_3, a large suppression was noted upon the addition of IPA. As such, $HO^•$ was shown to be the main oxidation specie in pure TiO_2 and WO_3 photocatalysis systems. The photocatalytic systems with added EDTA showed similar degradation rates compared to the system without scavengers, suggesting a limited role played by holes in the valence band. This may, in part, due to these reactions proceeding via reactions with OH^-, which is presumed to be in short supply at pH 5.

Additionally, these studies suggest multiple mechanisms are at play in the degradation of MB and RhB dyes, with further studies being done to confirm this. Two major active species' in the photodegradation process of MB and RhB dyes in the presence of $TiO_2/BiVO_4$ composite were seen, $O_2^{•-}$ and $HO^•$, while the main species of $CeO_2/BiVO_4$ and $BiVO_4/WO_3$ composite systems were $O_2^{•-}$ and $HO^•$, respectively. The generation of these radical species is explained in the context of their band edge energies, with the conduction band edge energies confirmed by Mott-Schottky measurements (Fig. S11) and valence band edges inferred based on optical bandgaps (see Fig. 6, Fig. S12 and Table S2). These experiments also highlight the possibility of a photocatalyst system being poisoned, a challenge which must be addressed in any real-world application of this technology.

Figure 6 shows the normalised rate constants for photodegradation of MB dye over the different photocatalysts under monochromatic light (using band pass filters) along with their absorption spectra. MB was chosen for this study as its absorption has little overlap with that of the photocatalysts in question, as opposed to RhB. As expected, in the absence of any catalyst (Fig. 6a) MB degraded most rapidly under 650 ± 20 nm light, close to its maximum absorption (664 nm) as a result of direct photolysis (mechanism 1, from Fig. 2a)[22, 41, 42]. A similar response to these wavelengths were seen with all catalysts as well. As was mentioned previously, mechanism (1) degradation should be largely independent of the catalyst used, while mechanism (2, specifically 2i in this case)

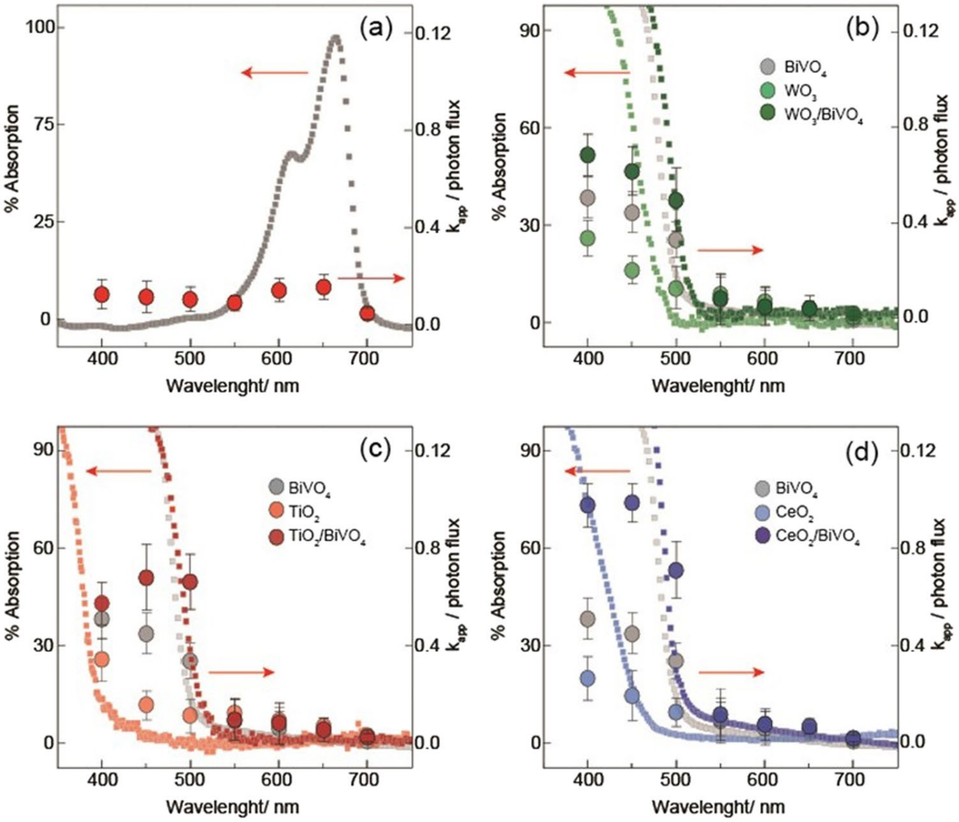

Figure 6. Absorption spectra of photocatalysts, and photocatalytic degradation rate of MB (k_{app}) as a function of wavelength (±20 nm band pass filters used), normalised against photon flux; (**a**) no catalyst; (**b**) WO_3, WO_3/$BiVO_4$ and $BiVO_4$; (**c**) TiO_2, TiO_2/$BiVO_4$ and $BiVO_4$; and (**d**) CeO_2, CeO_2/$BiVO_4$ and $BiVO_4$.

will be influenced by the chemical potential of free electrons in the CB. It is therefore concluded that that mechanism (2) plays a minor role, if at all, in the total photodegradation process here.

The absorption onsets of the WO_3, TiO_2 and CeO_2 were found to be 500, 390 nm and 435 nm respectively, while the absorption onset of all composites were dictated by that of $BiVO_4$, at about 525 nm (shown in Fig. 6b–d). It is seen that the main mechanism of MB degradation in each case is due to the photogeneration of reactive radical species. As mentioned above, composite formation is shown to have synergistic effect on degradation rates, suggesting effective interactions between the various metal oxide species.

For each composite, the responses to light of higher than band gap energies were enhanced as compared to the individual components, however this was more dramatic for some cases than others. As mentioned previously, $BiVO_4$ was selected as the common material as this results in equivalent total light harvesting for the composites. This hypothesis was validated looking at the absorption onsets of the composites, which were all indeed close to that of pure $BiVO_4$. This also provides us with the ability to deconvolute the responses of the coupled materials. At 500 nm $BiVO_4$ absorbs, whereas CeO_2 or TiO_2 do not (this is within the range of the absorption onset for WO_3, however direct comparison the response to this 500 nm light, as compared to 400 nm or 450 nm, where WO_3 more strongly absorbs light, is illustrative). Interestingly, while all composites showed a synergistic response at this wavelength, in the case of TiO_2 and WO_3, shorter wavelengths (400 and 450 nm) result in less marked differences as compared to pure $BiVO_4$. On the other hand, CeO_2 displays similar synergistic behaviour at all wavelengths from 400 to 500 nm.

Based on the combined results of quenching studies, monochromatic illumination Mott-Schottky experiments (Fig. S11) and optical band gap measurements (Fig. S12), the primary degradation mechanisms are proposed for the individual materials and WO_3/$BiVO_4$, TiO_2/$BiVO_4$, and CeO_2/$BiVO_4$ composites and are shown in Fig. 7. As mentioned, the main photodegradation mechanism seen with $BiVO_4$ involves the transfer of a photoexcited e^- from the CB of $BiVO_4$, along with a proton, to adsorbed an O_2 on the semiconductor surface, generating $HO_2^{\bullet}$.

Meanwhile, quenching studies showed $OH^{\bullet}$ to the only major reaction species for the pure WO_3 photocatalyst system, which be produced by oxidation at VB of WO_3. As OH^- exists only at low concentrations in slightly acid conditions, the photocatalytic activity exhibited here was lower than other materials. For the WO_3/$BiVO_4$ composite, (Fig. 7e) the CB and VB band edges of $BiVO_4$ are more negative than the CB and VB of the other component. Both $BiVO_4$ and WO_3 can be activated by visible light irradiation and generated e^- and h^+ pairs, although at 500 ± 20 nm, the relative portion of light harvested by the WO_3 should be considerably less compared to $BiVO_4$ than under 400 or 450 nm illumination.

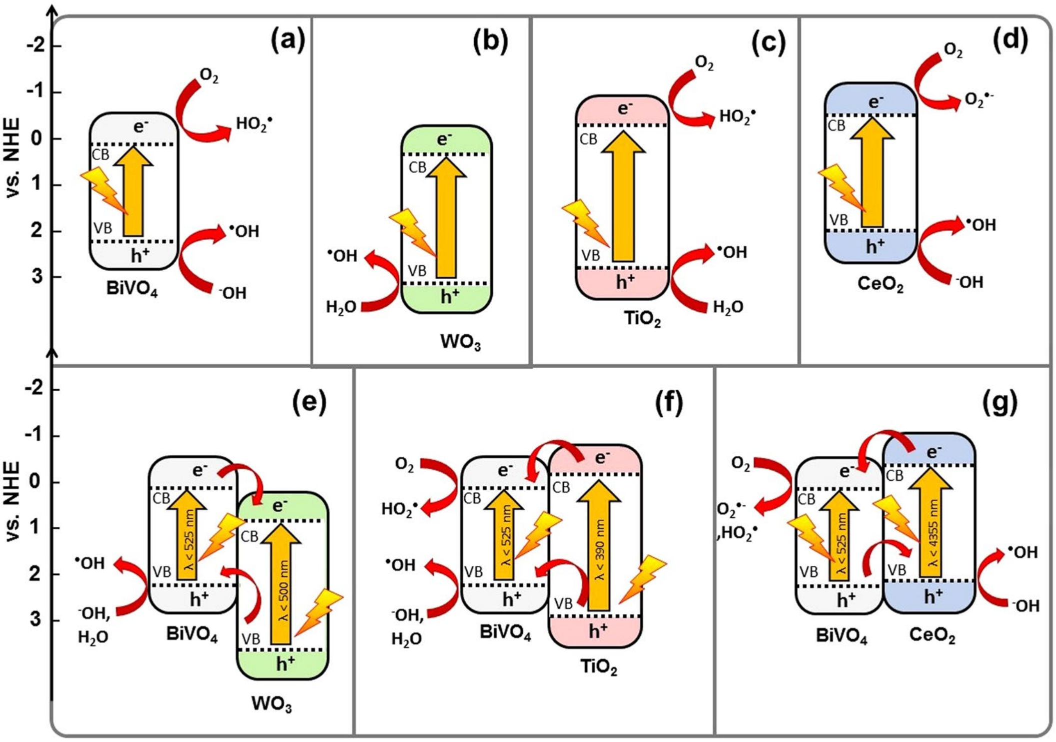

Figure 7. The proposed photocatalytic dye degradation mechanism in the presence of (**a**) $BiVO_4$, (**b**) WO_3, (**c**) TiO_2, (**d**) CeO_2, (**e**) $WO_3/BiVO_4$, (**f**) $TiO_2/BiVO_4$, and (**g**) $CeO_2/BiVO_4$ composites, irradiated under simulated solar light.

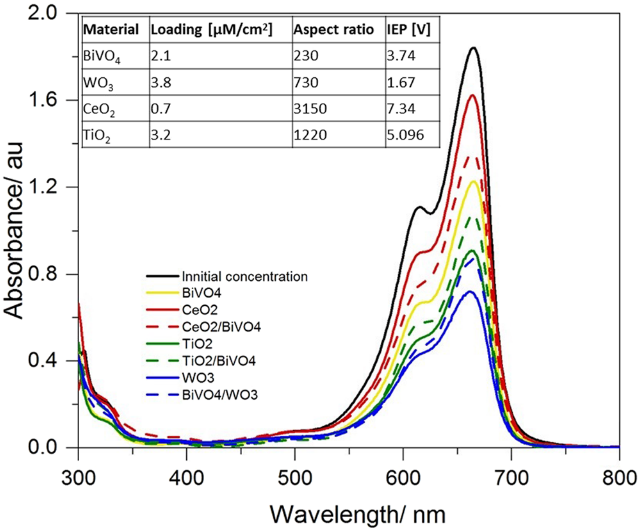

Material	Loading [μM/cm²]	Aspect ratio	IEP [V]
$BiVO_4$	2.1	230	3.74
WO_3	3.8	730	1.67
CeO_2	0.7	3150	7.34
TiO_2	3.2	1220	5.096

Figure 8. The absorption of MB solutions after being allowed to reach an adsorption-desorption equilibrium with the various photocatalyst films, overnight and in the dark. Inset compares the calculated dye loadings on the materials with their aspect ratios and isoelectric points (IEP).

According to the band edge analysis, electrons transferred to the CB of WO_3 cannot reduce O_2 to form radical species, as they can from the $BiVO_4$ CB. This is reflected in quenching studies, with the deactivation of the $O_2^{-•}$ species mechanism in $BiVO_4$ as it is paired with WO_3, representing an unintended consequence of composite formation. On the other hand, the photo-generated h^+ at the VB of WO_3 can transfer to the VB of $BiVO_4$, which can oxidize H_2O and HO^- to $HO^•$. Adding to the complex combination of effects in the composite, the dye is seen to have a very strong affinity towards WO_3. This is further explored by inspection of adsorption/desorption equilibrium of the dye, as measured in the dark (MB in Fig. 8 and RhB in Fig. S13), which shows the affinity of the dye towards WO_3 to be quite strong as compared to $BiVO_4$. In spite of an overall increased photocatalytic performance of the composite, as compared to pure WO_3 or pure $BiVO_4$, it can be seen that the mechanism of this enhancement is not straight forward. A similar trend was seen for RhB (see Fig. S13).

The role of surface area and isoelectric points (IEP) was explored (Fig. 8 above, as well as Fig. S14). This shows dye loading to be (1) highly dependent upon the materials' isoelectric point and (2) for composites, loading is close to a stoichiometric mixture of the loading of the individual component materials. The effect of the affinity for the dye for the various metal oxides is pivotal towards our understanding of the photocatalytic behaviour of composites, as described in the following paragraphs.

Under illumination TiO_2, can generate $HO^\bullet$ by reaction of adsorbed H_2O and h^+ in its VB. Additionally, adsorbed O_2 can produce $O_2^{\bullet-}$, by reaction with free e^- in the CB. Figure 7f shows the mechanisms observed in $BiVO_4/TiO_2$ composites, where the CB and VB of $BiVO_4$ are both located between the CB and VB of TiO_2. This represents an interesting case, particularly under 450 nm and 500 nm illumination, where only $BiVO_4$ is photoexcited and there are no obvious pathways whereby CT to TiO_2 can occur. Photocatalytic performance is however substantially higher than for pure $BiVO_4$. This appears to again stem from the affinity of the dye for TiO_2, whereby a high concentration of these dyes is maintained in proximity to the $BiVO_4$ catalyst, which is the primary producer of the active radical species. This affinity is seen in the dark adsorption/desorption equilibrium (Fig. 8) and explained by the by the zeta potential of TiO_2 (Fig. S14). Thus, the major process of this system should be driven by the visible light havering of $BiVO_4$ which can produce $HO_2^\bullet$ and/or $O_2^{\bullet-}$ at its CB.

As CeO_2 has a higher CB edge potential than $BiVO_4$, free electrons have a substantial free energy to generate $O_2^{\bullet-}$ from O_2, which was seen to be the main photocatalytic mechanism at play here (Fig. 7d). The comparatively low photocatalytic activity of CeO_2 (versus $BiVO_4$) is in part attributed to low visible light absorption. 400 nm monochromatic illumination shows however that this is not the only factor, along with dark adsorption/desorption measurements (Fig. 8) which reveal the low affinity of the dye for CeO_2, despite its high surface area. As seen in Fig. 7g, the CB and VB potential edges of $BiVO_4$ are more positive than those of CeO_2. The tendency of CT is that photoexcited e^- in the CB of CeO_2 can be transferred to $BiVO_4$, where they can react with absorbed O_2 to create $O_2^{\bullet-}$ radicals. From the quenching studies, $HO^\bullet$ was also observed to play role in this system, suggesting that these $HO^\bullet$ were probably generated from intermediate species and/or the generated $O_2^{\bullet-}$ and $HO_2^\bullet$ radicals[22, 24]. Therefore, the main mechanism is production of $HO^\bullet$ at the VB of the $BiVO_4$ in the composite that leads to showing the lowest photocatalytic activity as compared to the $CeO_2/BiVO_4$ and $TiO_2/BiVO_4$ composites.

Discussion

A series of composites were constructed, containing WO_3, TiO_2 or CeO_2 with $BiVO_4$. This last component ensured each system had similar overall light harvesting. XRD, XPS, SEM and TEM analyses confirm the formation of the composite without significant doping. Furthermore, highly porous films were formed, with a good dispersion of the different materials among each other.

Superior photocatalytic performance for degradation of MB and RhB under simulated solar light irradiation was observed for all composites, relative to their component materials. Monochromatic illumination and active species quenching studies were conducted and revealed a great deal of information about the different routes by which radical species were produced, leading to the degradation of these dyes. Quenching studies, indicated that $O_2^{\bullet-}$ is a main reactive specie generated by $CeO_2/BiVO_4$ systems, while $BiVO_4/WO_3$ primarily degraded dyes via $HO^\bullet$, and both $O_2^{\bullet-}$ and $HO^\bullet$ were active for the $TiO_2/BiVO_4$ composite.

Typically enhanced free carrier lifetimes resulting from a spatial separation of charges in different (neighbouring) materials is cited as a reason for enhanced performance, however here we see a number of other factors also had a bearing on the behaviour of composite systems. Specifically, it was seen that the affinity of the dye to the partner semiconductor plays a major role as it provides a high local concentration, where generated radicals have a higher probability of being able to react as compared to in the general solution. This was demonstrated clearly in the case the $BiVO_4$-TiO_2 composite, under 450 and 500 nm illumination of where no CT mechanisms are favourable, yet the degradation rate constant is roughly twice as large as for pure $BiVO_4$. The WO_3-$BiVO_4$ composite was also seen to be an interesting case, with the band edge configuration deactivating one radical species generation pathway. Again, the overall performance increased, which again be attributable to high dye affinity for WO_3.

This study highlights the complexities of composite design for photocatalysis, and the need to consider a range of factors, such as zeta potential and surface area, when designing new systems. It also demonstrated that band edge offsets can lead to deactivation of radical species generating pathways, as well as the more desirable increase in free charge carrier lifetime. We hope that it can serve as a basis for further design of new composite materials for water purification and other applications.

Methods

Preparation of photocatalyst powder. The synthesis of all photocatalysts were carried out by solution phase synthetic methods. For the synthesis of $BiVO_4$ powder, bismuth nitrate and ammonium vanadate in dilute nitric acid solution were used as starting precursors for precipitation at room temperature. $CeO_2/BiVO_4$ and $TiO_2/BiVO_4$ composites were prepared by two-step methods[20, 43]. Firstly, $BiVO_4$ powder was synthesised by a precipitation method. Subsequently the $BiVO_4$ powder was added into either cerium nitrate or titanium isopropoxide solutions to prepare composites by precipitation or sol-gel methods, respectively. $BiVO_4/WO_3$ composites were also synthesised by a two-step precipitation method, where WO_3 powder was first synthesised using tungsten nitrate as the starting material. The WO_3 powder was added into a solution with of Bi and V precursors. The choice of synthetic order relates to pH regulation for each step and stability of the partner material under these conditions. Detailed descriptions of the synthesis of each of the $CeO_2/BiVO_4$, $TiO_2/BiVO_4$ and $BiVO_4/WO_3$ composites in the supporting information.

Fabrication of photocatalyst films. All films for photocatalytic testing and electrochemical measurements were prepared by a doctor blading technique[29]. Briefly, 0.5 g of the photocatalyst powder was used, along with 75 µL Triton X-100, 25 µL acetic acid and 4 mL ethanol. The slurry was ground with a mortar and pestle for 10 min, during which ethanol was added in small aliquots to break up larger agglomerates. The paste was then sonicated for a further 30 min. Films were obtained by blading the slurry (~100 µL) on either glass slides (film size = 20 mm × 40 mm) for photocatalytic experiment or (~12.5 µL) on FTO glass working electrodes (film size = 10 mm × 10 mm) for Mott-Schottky experiment. This was carried out on a heated (50 °C) surface, using Scotch Tape (3 M, 50 µm) as a spacer. These films were then annealed in air at 450 °C for 2 h, to produce mechanically stable films. The thicknesses of the resulting films were 2.8 ± 0.1 µm, as measured with a stylus profilometer (VeecoDektak 150).

Physical characterization of photocatalyst materials. X-Ray Diffractometry (JDX-3530, JEOL, Japan) was completed using Cu K_α radiation ($\lambda = 1.546$ nm). The detection range was 10° and 70° with the step size of 0.2° (2θ/s) in continuous scanning mode. Film morphologies were investigated by a Scanning Electron Microscope (SEM, JSM-7500FA, JEOL, Japan) with the accelerating voltage and emission current as 5.0 kV and 10 µA, respectively. The chemical composition and electron structure of the bare CeO_2, $BiVO_4$ and $BiVO_4/CeO_2$ composite were measured by X-ray photoelectron spectroscopy (XPS, PHOIBOS 100 hemispherical energy analyser from SPECS) using Al, K_α radiation (1486.6 eV) in fixed analyser transmission mode. The binding energies were calibrated with reference to C 1 s line at 284.6 eV for hydrocarbon contamination

Films were optically characterized using a Shimadzu 3600 UV-Vis-NIR spectrophotometer, with integrating sphere attachment. Transmission and reflection measurements were made in order to determine the absorption. Images were taken on an FEI Helios G3 CX using the STEM3 + detector at 30 kV. EDS data was acquires using an Oxford instruments X-max^N 150 mm^2 SDD detector with acquisition and processing performed with the AZtec application suite. Samples were prepared by sonicating a dilute dispersion of the material in ethanol and dropping on a carbon coated copper grid.

Photocatalytic testing. Photocatalytic activities of the synthesized photocatalyst powder and films were studied by the degradation of either Rhodamime B (~25 µM, RhB) or methylene blue (~50 µM, MB) solutions under simulated solar illumination (AM1.5 G, 1 sun equivalent, 100 mW cm^{-2}). For monochromatic experiments, ±20 nm band pass filters were applied to the above light source.

Photocatalyst films were placed put in a reactor with the dye solution. Prior to irradiation, the films were left overnight in the dye solution under continuous magnetic stirring in order to attain an adsorption/desorption equilibrium. At irradiation time intervals of 30 min, the dye solution was collected and measured using an UV-vis spectrophotometer (Agilent 8453 photodiode array). After that, the collected solution was put back into the reactor, and the photodegradation reaction resumed (<3 min intermission).

An indirect chemical probe method was employed to investigate the mechanisms of dye degradation. Scavengers of various possible active species, including isopropanol (IPA, an $HO^\bullet$ quencher), benzoquinone (BQ, $O_2^{\bullet -}$ quencher) and ethylenediamine tetra acetic acid (EDTA, a h^+ scavenger), were added at 1 mM during the photoreaction[35–40].

Each experiment was repeated in triplicate, with the average value shown along with one standard deviation as an error bar.

References

1. Kudo, A. & Miseki, Y. Heterogeneous Photocatalyst Materials for Water Splitting. *Chem. Soc. Rev.* **38**, 253–278 (2009).
2. Bhatkhande, D. S., Pangarkar, V. G. & Beenackers, A. A. C. M. Photocatalytic Degradation for Environmental Applications: A Review. *J. Chem. Technol. Biotechnol.* **77**, 102–116 (2002).
3. Wang, D. *et al.* Photocatalytic Water Oxidation on $BiVO_4$ with the Electrocatalyst as an Oxidation Cocatalyst: Essential Relations between Electrocatalyst and Photocatalyst. *J. Phys. Chem. C.* **116**, 5082–5089 (2012).
4. Pelaez, M. *et al.* A Review on the Visible Light Active Titanium Dioxide Photocatalysts for Environmental Applications. *Appl. Catal., B.* **125**, 331–349 (2012).
5. Abdi, F. F., Savenije, T. J., May, M. M., Dam, B. & Krol, R. The Origin of Slow Carrier Transport in $BiVO_4$ Thin Film Photoanodes: A Time-Resolved Microwave Conductivity Study. *J. Phys. Chem. Lett.* **4**, 2752–2757 (2013).
6. Gupta, S. & Tripathi, M. A Review of TiO_2 Nanoparticles. *Chin. Sci. Bull.* **56**, 1639–1657 (2011).
7. Ahmed, S., Rasul, M. G., Martens, W. N., Brown, R. & Hashib, M. A. Heterogeneous Photocatalytic Degradation of Phenols in Wastewater: A Review on Current Status and Developments. *Desalination.* **261**, 3–18 (2010).
8. Li, L. & Yan, B. $BiVO_4/Bi_2O_3$ Submicrometer Sphere Composite: Microstructure and Photocatalytic Activity under Visible-light Irradiation. *J. Alloys Compd.* **476**, 624–628 (2009).
9. Chen, L. *et al.* Porous Peanut-like $Bi_2O_3/BiVO_4$ Composites with Heterojunctions: One-step Synthesis and Their Photocatalytic Properties. *Dalton Trans.* **41**, 9513–9518 (2012).
10. Jiang, H., Nagai, M. & Kobayashi, K. Enhanced Photocatalytic Activity for Degradation of Methylene Blue over $V_2O_5/BiVO_4$ Composite. *J. Alloys Compd.* **479**, 821–827 (2009).
11. Hong, S. J., Lee, S., Jang, J. S. & Lee, J. S. Heterojunction $BiVO_4/WO_3$ Electrodes for Enhanced Photoactivity of Water Oxidation. *Energy Environ. Sci.* **4**, 1781–1787 (2011).
12. Hu, Y. *et al.* $BiVO_4/TiO_2$ Nanocrystalline Heterostructure: A Wide Spectrum Responsive Photocatalyst towards the Highly Efficient Decomposition of Gaseous Benzene. *Appl. Catal., B.* **104**, 30–36 (2011).
13. Zhang, L. *et al.* Microwave Hydrothermal Synthesis and Photocatalytic Properties of $TiO_2/BiVO_4$ Composite Photocatalysts. *Ceram. Int.* **39**, 8597–8604 (2013).
14. Chatchai, P., Murakami, Y., Kishioka, S. Y., Nosaka, A. Y. & Nosaka, Y. Efficient Photocatalytic Activity of Water Oxidation over $WO_3/BiVO_4$ Composite under Visible Light Irradiation. *Electrochim. Acta.* **54**, 1147–1152 (2009).
15. Chatchai, P., Nosaka, A. Y. & Nosaka, Y. Photoelectrocatalytic Performance of $WO_3/BiVO_4$ toward the Dye Degradation. *Electrochim. Acta.* **94**, 314–319 (2013).
16. Su, J., Guo, L., Bao, N. & Grimes, C. A. Nanostructured $WO_3/BiVO_4$ Heterojunction Films for Efficient Photoelectrochemical Water Splitting. *Nano Lett.* **11**, 1928–1933 (2011).

17. Jiang, J., Wang, M., Li, R., Ma, L. & Guo, L. Febricating CdS/$BiVO_4$ and $BiVO_4$/CdS Heterostructured Film Photoelectrodes for Photoelectrochemical Applications. *Int. J. Hydrogen Energy.* **38**, 13069–13076 (2013).
18. Bajaj, R., Sharma, M. & Bahadur, D. Visible Light-driven Novel Nanocomposite ($BiVO_4$/$CuCr_2O_4$) for Efficient Degradation of Organic Dye. *Dalton Trans.* **42**, 6736–6744 (2013).
19. Pilli, S. K. *et al.* $BiVO_4$/$CuWO_4$ Heterojunction Photoanodes for Efficient Solar Driven Water Oxidation. *Phys. Chem. Chem. Phys.* **15**, 3273–3278 (2013).
20. Wetchakun, N. *et al.* $BiVO_4$/CeO_2 Nanocomposites with High Visible-Light-Induced Photocatalytic Activity. *ACS Appl. Mater. Interfaces.* **4**, 3718–3723 (2012).
21. Liqiang, J. *et al.* Review of Surface Photovoltage Spectra of Nanosized Semiconductor and Its Applications in Heterogeneous Photocatalysis. *Sol. Energ. Mat. Sol. Cells* **79**, 133–151 (2003).
22. Armstrong, D. A. *et al.* Standard electrode potentials involving radicals in aqueous solution. *Pure Appl. Chem.* **87**, 1139–1150 (2015).
23. Linsebigler, A. L., Lu, G. & Yates, J. T. Photocatalysis on TiO_2 Surfaces: Principles, Mechanisms, and Selected Results. *Chem. Rev.* **95**, 735–758 (1995).
24. Ajmal, A., Majeed, I., Malik, R. N., Idriss, H. & Nadeem, M. A. Principles and Mechanisms of Photocatalytic Dye Degradation on TiO_2 Based Photocatalysts: A Comparative Overview. *RSC Adv.* **4**, 37003–37026 (2014).
25. Hennig, H. Semiconductor Photocatalysis: Principles and Applications. *Chem. Int. Ed.* **54**, 4429–4429 (2015).
26. Nishimoto, S., Mano, T., Kameshima, Y. & Miyake, M. Photocatalytic Water Treatment over WO_3 under Visible Light Irradiation Combined with Ozonation. *Chem. Phys. Lett.* **500**, 86–89 (2010).
27. Liu, W., Wang, M., Xu, C., Chen, S. & Fu, X. An Efficient Visible-light-sensitized Composite with Its Application in Photocatalytic Degradation of Rhodamine B. *Mater. Res. Bull.* **48**, 106–113 (2013).
28. Sun, M., Su, Y., Du, C., Zhao, Q. & Liu, Z. Self-doping for Visible Light Photocatalytic Purposes: Construction of SiO_2/SnO_2/SnO_2:Sn^{2+} Nanostructures with Tunable Optical and Photocatalytic Performance. *RSC Adv.* **4**, 30820–30827 (2014).
29. Wetchakun, N., Incessungvorn, B., Wetchakun, K. & Phanichphant, S. Influence of Calcination Temperature on Anatase to Rutile Phase Transformation in TiO_2 Nanoparticles Synthesized by the Modified Sol-gel Method. *Mater. Lett.* **82**, 195–198 (2012).
30. Kumar, K. V., Porkodi, K. & Rocha, F. Langmuir Hinshelwood Kinetics – A Theoretical Study. *Catal. Commun.* **9**, 82–84 (2008).
31. Naik, B., Martha, S. & Parida, K. M. Facile fabrication of Bi_2O_3/$TiO_{2-x}N_x$ Nanocomposites for Excellent Visible Light Driven Photocatalytic Hydrogen Evolution. *Int. J. Hydrogen Energy* **36**, 2794–2802 (2011).
32. Gurulakshmi, M. *et al.* Enhanced Visible Light Photocatalytic Activity of V_2O_5/S-TiO_2 Nanocomposites. *Appl. Catal., A.* **449**, 31–46 (2012).
33. Li, H., Wu, C. Y., Li, Y. & Zhang, J. Superior Activity of MnO*x*-CeO_2/TiO_2 Catalyst for Catalytic Oxidation of Elemental Mercury at Low Flue Gas Temperatures. *Appl. Catal., B.* **111–112**, 381–388 (2012).
34. Watanabe, S., Ma, X. & Song, C. Characterization of Structural and Surface Properties of Nanocrystalline TiO_2-CeO_2 Mixed Oxides by XRD, XPS, TPR, and TPD. *J. Phys. Chem. C* **113**, 14249–14257 (2009).
35. Minero, C., Mariella, G., Maurino, V., Vione, D. & Pelizzetti, E. Photocatalytic Transformation of Organic Compounds in the Presence of Inorganic ions. 2. Competitive Reactions of Phenol and Alcohols on a Titanium Dioxide-fluoride System. *Langmuir* **16**, 8964–8972 (2000).
36. Zhang, H., Zong, R., Zhao, J. & Zhu, Y. Dramatic Visible Photocatalytic Degradation Performances Due to Synergetic Effect of TiO_2 with PANI. *Environ. Sci. Technol.* **42**, 3803–380 (2008).
37. Bandara, J. & Kiwi, J. Fast Kinetic Spectroscopy, Decoloration and Production of H_2O_2 Induced by Visible Light in Oxygenated Solutions of the Azo Dye Orange II. *New J. Chem.* **23**, 717–724 (1999).
38. Baciocchi, E. *et al.* Electron Transfer and Singlet Oxygen Mechanisms in the Photooxygenation of Dibutyl Sulfide and Thioanisole in MeCN Sensitized by N-Methylquinolinium Tetrafluoborate and 9,10-Dicyanoanthracene. The Probable Involvement of a Thiadioxirane Intermediate in Electron Transfer Photooxygenations. *J. Am. Chem. Soc.* **125**, 16444–16454 (2003).
39. Mrowetz, M. & Selli, E. Enhanced Photocatalytic Formation of Hydroxyl Radicals on Fluorinated TiO_2. *Phys. Chem. Chem. Phys.* **7**, 1100–1102 (2005).
40. Sun, Y. & Pignatello, J. J. Evidence for a Surface Dual Hole- Radical Mechanism in the Ti02 Photocatalytic Oxidation of 2,4 = Dichlorophenoxyacetic Acid. *Environ. Sci. Technol.* **29**, 2065–2072 (1995).
41. Kamat, P. V. Photoelectrochemistry in Colloidal Systems. Part 2.–A Photogalvanic Cell Based on TiO_2 Semiconductor Colloid. *J. Chem. Soc. Faraday Trans.* **81**, 509–518 (1985).
42. Takizawa, T., Watanabe, T. & Honda, K. Photocatalysis through Excitation of Adsorbates. 2. A Comparative Study of Rhodamine B and Methylene Blue on Cadmium Sulfide. *J. Phys. Chem. A.* **82**, 1391–1396 (1978).
43. Nattestad, A., Ferguson, M., Kerr, R., Cheng, Y. B. & Bach, U. Dye-sensitized Nickel(II) Oxide Photocathodes for Tandem Solar Cell Applications. *Nanotechnology.* **19**, 29 (2008).

Acknowledgements

The authors gratefully acknowledge the financial support from Thailand Graduate Institute of Science and Technology (TGIST) Grant (TG 01–54–088) for K.P. and National Nanotechnology Centre (NANOTEC), The National Science and Technology Development Agency (NSTDA). A.N. would like to thank the Australian Renewable Energy Network (ARENA) and the Australian Research Council (DE160100504) for funding. We also thank the Australian National Fabrication Facility (ANFF), ARC Centre of Excellence for Electromaterials (ACES), and The Electron Microscopy Centre (EMC) at University of Wollongong (Australia) for the facility support, the National Research University Project under Thailand's Office of the Higher Education Commission, and Department of Chemistry, Faculty of Science, Chiang Mai University.

Author Contributions

K.P. performed the bulk of the experimental work, with some assistance from A.N. The Manuscript was prepared by K.P., J.C. and A.N. with input from W.K., G.G.W. and S.P.

Additional Information

Supplementary information accompanies this paper at doi:10.1038/s41598-017-09514-5

Competing Interests: The authors declare that they have no competing interests.